Mass transfer in the wake of non-spherical air bubbles quantified by quenching of fluorescence

Mélanie Jimenez, Nicolas Dietrich, Gilles Hébrard

MASS TRANSFER IN THE WAKE OF NON SPERICAL AIR BUBBLES QUANTIFIED BY QUENCHING OF FLUORESCENCE

M. Jimenez[a,b,c,d*], N. Dietrich[a,b,c,d], G. Hébrard[a,b,c,d]

[a] Université de Toulouse; INSA, UPS, INP; LISBP, 135 Av. de Rangueil, F-31077 Toulouse, France

[b] INRA UMR792, Ingénierie des Systèmes Biologiques et des Procédés, F-31400 Toulouse, France

[c] CNRS UMR 5504, Ingénierie des Systèmes Biologiques et des Procédés, F-31400 Toulouse, France

[d] Fédération de recherche FERMAT, CNRS, Toulouse, France

(*Corresponding Author's E-mail: mjimenez@insa-toulouse.fr)

Keywords: PLIF; bubble; gas/liquid interface

ABSTRACT

Based on PLIF experiments, the mass transfer behavior in the wake of single rising air bubbles has been investigated. Bubbles of equivalent diameters between about 0.7 and 2mm have been studied, corresponding to vertical and zigzagging paths respectively. The mass transferred in the wake of such bubbles, considered as spherical or oblate ellipsoids, has been directly visualized and its three dimensional representation has been performed for some of them. A specific image processing and mathematical approach have been proposed to accurately quantify the mass transfer by mean of liquid side mass transfer and flux density measurements. After a comparison of liquid side mass transfer coefficients with literature, this approach has been tested to evaluate the impact of first bubble diameters and then the liquid composition on the mass transfer. Liquid media with small amount of salt, glucose and glycerol have been

considered, inducing surface tension and/or viscosity changes. A significant difference in the mass transfer behavior has been observed depending on the liquid composition, thus decreases down to 88% of the mass transferred by the bubble have been obtained due to this composition difference.

1. Introduction

Gas/liquid mass transfer causes searchers no end of trouble. Despite the numerous studies devoted to understand this phenomenon, several questions remain, especially because of the complexity of the different mechanisms occurring at the vicinity of the gas/liquid interface.

When considering the specific case of bubble system, which is the main purpose of this paper and represents, as well known, a large part of industrial applications dealing with gas/liquid mass transfer, difficulties are many-sided. In such a system, the dissolution of a given gas in the liquid phase relies on the on the hydrodynamic behavior (linked to the bubble diameter, shape, velocity, trajectory, presence of other bubbles, *etc.*), the gas system (gas solubility in the liquid phase), the liquid composition (presence of surfactants, viscous media…), operating conditions (temperature, pressure) and so on. The main challenge consists thus of isolating a specific parameter and accurately analyzing its influence on the mass transfer mechanism. However, in several industrial processes (aeration, BCR, *etc.*), the gas phase is usually considered as bubble swarms with potentially gas volume fraction up to 20% (Colombet *et al.*, 2011). The gas/liquid mass transfer characterization in these configurations is thus usually restricted to a global approach (Calderbank and Lochiel, 1964) for instance by

measuring the evolution of the dissolved gas concentration in the liquid phase which limits the understanding of the local phenomena. As an example of this limitation based on numerical simulations, Koynov *et al.* (2005) have demonstrated that both hydrodynamic and mass transfer behaviors are influenced by the presence of several bubbles (see also Bothe and Warnecke, 2005). For this reason, more academic cases involving single bubbles have been largely accepted as a first and inevitable step. Moreover, a recent study conducted by Colombet *et al.* (2011) in the characterization of liquid side mass transfer coefficients k_L in dense bubble swarms (gas volume fraction ranging from 0.45 to 16.5%) has demonstrated that the collective effect does not significantly impact k_L values since mass transfer occurs within a very thin layer (some micrometers) located at the front of the bubble. Focusing on single bubble configuration is indeed a relevant approach for gas/liquid mass transfer characterization.

To locally analyze hydrodynamic, mass transfer or both in this simplified configuration, numerous and ingenious techniques have appeared. Some of them are based on the use of probe/microprobe. For instance, Riethues *et al.* (1986) performed local dissolved oxygen measurements using oxygen microprobe by fixing an air bubble with a platinum wire spiral. More recently, Hanyu and Saito (2010) proposed a photoelectric optical fiber probe to accurately determine CO_2 concentrations in the bubble wake but also bubble diameter and velocity. However, such systems are still limited to a specific location (Brücker, 1999) and usually considered as intrusive methods. To perform more suitable measurements, another class of techniques, based on direct visualization, distinguished itself from the others. Such techniques are

commonly based on optical systems allowing a direct visualization of the phenomenon of interest. In a simple manner, bubble trajectory, shape and velocity can be determined using high speed camera for instance (Bel Fdhila and Duineveld, 1996, Zhang *et al.,* 2003; Alves *et al.*, 2005; Madhavi *et al.,* 2007). Purposes dealing with bubble size decrease due to the mass transfer can also be considered (Alves *et al.*, 2005; Madhavi *et al.,* 2007). Still based on the use of cameras, some techniques allow the visualization of other phenomenon such as the bubble wake (dye-based visualization by Lunde and Perkins (1997), schlieren optics techniques by de Vries *et al.*, (2002) for instance). However, laser-based techniques represent one of the main powerful approach to accurately visualize local phenomenon occurring during the bubble rise and transfer. Examples of such techniques are for instance Particle Image Velocimetry (Lindken and Merzkirch, 2000; Yamamoto *et al.*, 2008; Tachibana and Saito, 2010), photochromatic dye-based technique (Sanada *et al.*, 2007) for the visualization of the hydrodynamic behavior in the bubble wake. Concerning the characterization of the mass transfer, techniques are scarcer and most of studies are based on Planar Laser Induced Fluorescence (PLIF) even if holographic interferometry can also be used (Ma *et al.*, 1999). PLIF allows direct visualization in liquid phases by adding a fluorescent dye whose fluorescence intensity depends on changes of specific parameters in the liquid phase (gas concentration, pH or temperature for instance). Since the 90s, this technique has been widely used to visualize but also to quantify the mass transfer in gas/liquid systems through planar/wavy interfaces (Wolff *et al.*, 1991; Herlina and Jirka, 2004; Jimenez *et al.,* 2012) or bubble interface (Bork *et al.*, 2005; Dani *et al.*, 2007; Stöhr *et al.*, 2009; Hanyu and Saito, 2010; Kück *et al.*, 2010). However concerning

bubbling systems, in most papers, experimental set ups limit the accurate quantification of mass transfer. Such a limitation is mainly due to the high reflection of the laser light on the bubble surface which could strongly alter concentration measurements and the presence of the bubble shadow in the opposite side of the laser flash. Moreover even if some papers deal with three dimensional PLIF (Stöhr *et al.*, 2009), most of PLIF applications are limited to a two-dimensional representation of the mass transfer in the bubble wake. Based on this 2-D characterization, the extrapolation of the whole mass transfer is not straightforward especially for asymmetric configurations where the mass transfer is usually shed in a tortuous way (Koynov *et al.*, 2005; Yamamoto *et al.*, 2008; Stöhr *et al.*, 2009). An example of such an extrapolation in an axisymmetric configuration is proposed by Kück *et al.* (2010). To avoid all these technical issues that hinder an accurate quantification of the mass transfer, a new approach based on a repositioning of the optical system has been proposed by François *et al.* (2011).

The proposed experimental set up allows the mass transfer to be visualized by PLIF along a horizontal plane, perpendicularly to the bubble rising direction, at successive instants. Based on the recorded images, the three-dimensional profile of the mass transfer in the wake of the bubble can easily be reconstructed and thus quantified. A specific mathematical approach has also been proposed to determine the main parameters characterizing the mass transfer such as the flux density j_{O_2} or the liquid side mass transfer coefficient k_L. This approach has been tested for different liquid viscosities (from 0.001 to 0.058 Pa.s) but has been limited to spherical bubbles following a rectilinear trajectory. Moreover, the bubble diameters considered in this

study do not allow a direct comparison between the different studied cases to clearly identify the impact of viscosity on the mass transfer.

The purpose of this paper is to extend the previous work of François *et al.* (2011) to more complex configurations to go beyond the understanding of gas/liquid mass transfer mechanisms. First, the paper focuses on the impact of diameter, shape and trajectory of rising bubbles on the visualized mass transfer. It can be noted that in the present paper, air bubbles are considered, contrary to pure oxygen bubbles in François *et al.* (2011), to be closer to main industrial purposes. Then an extension of the previous mathematical analysis is proposed for non-spherical configurations to quantify the mass transfer released by non-spherical bubbles. Finally, the impact of the liquid composition on both hydrodynamic and mass transfer but also on the fluorescence phenomenon has been investigated by considering the presence of salt, glucose and glycerol in the liquid phase.

2. Experimental set-up

2.1. PLIFI technique

The visualization of the mass transfer in the bubble wake is performed by the PLIFI (Planar Laser Induced Fluorescence with Inhibition) technique. The basic principle of the PLIF is to introduce in the liquid phase a fluorescent dye that will reemit light once excited by an appropriate light, usually generated by a laser source (Geddes,

2001; Crimaldi, 2008). When considering the PLIFI, the ability of some molecules called "quenchers" to inhibit the fluorescence phenomenon of the dye is considered. Oxygen molecule that is of prime interest in this study has been known as an excellent quencher for many years. This quenching effect is usually considered as a consequence of collisions between molecules where the excess of energy of the dye is absorbed by oxygen (Lakowicz, 1999). The appositeness of PLIFI is mainly due to the fact that it is not limited to visualization but allows also accurate quantification of mass transfer. Since the fluorescence level is directly related to the oxygen concentration in the liquid phase and using the Stern Volmer (1919) equation [1], it is straightforward to achieve the mass transfer quantification.

$$\frac{I_Q}{I_0} = \frac{1}{1 + K_{SV}[Q]} \quad [1]$$

where K_{SV} is the Stern-Volmer constant (L/mg), $[Q]$ the quencher concentration (mg/L), and I_Q and I_0 the fluorescence intensities in the presence and the absence of quencher, respectively. The parameters I_0 and K_{SV} of the calibration curve can be easily determined by fitting equation [1] with different recorded fluorescence intensities I_Q (or grey levels) corresponding to solutions of known and uniform oxygen concentration. The measurement of the dissolved oxygen concentration in the liquid is performed using specific probes (LE621 probe, Mettler Toledo, ±1%). An example of typical calibration curve is presented in **Figure 1**.

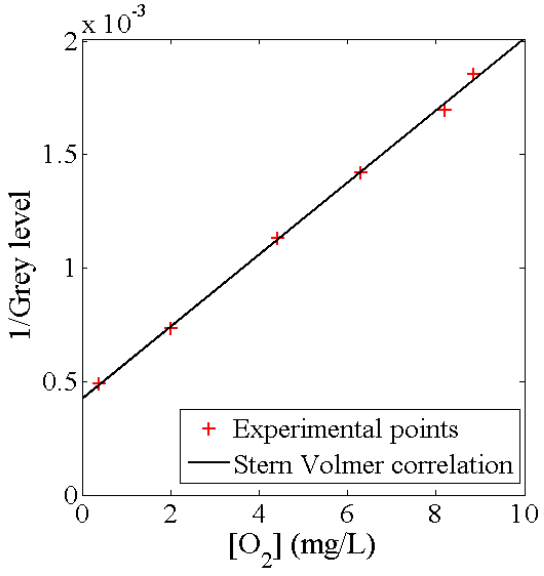

Figure 1- Calibration curve for a water-ethanol 20%w/w solution at 20°C with 25 mg/L of Ruthenium complex (I_0=2381, K_{SV}=0.366 L/mg)

For all the tested liquid media, the inverse proportionality between fluorescence level and oxygen concentration has been obtained with a square correlation coefficient higher than 99%.

2.2. Application of the PLIFI technique

The experimental set-up is quite similar to the one presented by François *et al.* (2011) and is depicted in **Figure 2**.

A single air bubble (3) is injected by a peristaltic pump and a capillary (2) into a transparent column (1) made of PMMA (Polymethyl Methacrylate) filled with the liquid of interest (water for instance) previously deoxygenated using nitrogen. To observe the mass transfer in the bubble wake (4), 25 mg/L of Ruthenium complex ($C_{72}H_{48}N_8O_6Ru$, Nanomeps) has been added to the liquid as fluorescent dye. The main advantage of this fluorescent dye is its high sensitivity to the presence of oxygen. As an example deduced from **Figure 1**, there is a difference of more than 1800 grey levels on the recorded images between fully and totally not oxygenated solutions

allowing a high accuracy for quantification. However, since it is not directly water-soluble, 20% w/w of ethanol has also been added to the media (Dani *et al.,* 2007). The impact of ethanol in the solution is discussed in Part 6- Results and Discussion. Other components have been also added to the liquid phase to test their influence on the mass transfer phenomenon. Characteristics of the different tested liquid media are presented in **Table 1**. These characteristics have been measured with a Haake VT550 Viscotester (ThermoScientific, Thermo Fisher Scientific, Inc.) for the viscosity, a pycnometer (Brand Duran, V=25 cm^3) for the density and a tensiometer (3S GBX) for the surface tension.

Composition		σ ($mN.m^{-1}$)	μ (Pa.s)	ρ ($kg.m^{-3}$)
Water		72.8	0,0010	995
Water + Ethanol 20%w/w + dye		38.9	0,0010	965
+ Salt	1 g/L	39.0	0,0010	965
	5 g/L	39.2	0,0010	969
+ Glucose	0.5 g/L	38.8	0,0010	964
	1g/L	39.1	0,0010	966
+ Glycerol	10% w/w	39.7	0,0013	988
	25% w/w	40.4	0,0019	1024

Table 1- Comparison of the properties of the considered liquid phases

Then, to excite the fluorescent dye, a laser sheet (6), is horizontally generated by a Nd: Yag laser (5) (Quantel, λ=532 nm, 10 Hz, 2×200 mJ) about 10 cm above the column bottom at 10 Hz. The fluorescence level in the wake of the bubble is recorded by a CCD camera (8) (Imager Intense, LaVision, Germany, 12 bits, 1040×1376 $pixels^2$) located under the column and focalizing where the laser flashes. A 105 mm objective (Micro-Nikkor 105 mm f/8, Nikon) and three teleconverters were added to the digital camera to obtain a focused area of about 3×4 mm^2. Since the Ruthenium complex emits around 670 nm, a 570 nm high-pass filter was also placed on the CCD camera to

register its fluorescence and to block the laser light. A high speed camera (11) (PCO 1200, 10 bits, 770 Hz,1024×1280 pixels²) is placed orthogonally to the first camera (8) and above the laser sheet (6) to record the velocity, the shape and the diameter of the bubble (image area ≈ 3×4 cm²). The laser and the CCD camera are synchronized by a Programmable Trigger Unit (LaVision) (9).

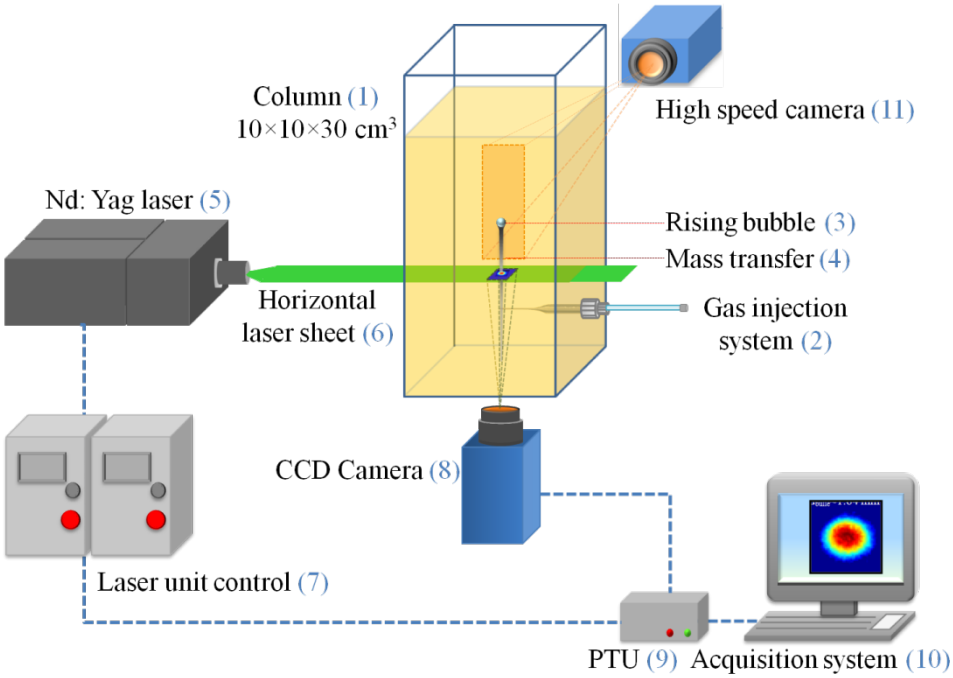

Figure 2- Experimental set-up for PLIF measurements

An example of typical sequence recorded by the CCD camera (8) is shown in **Figure 3**.

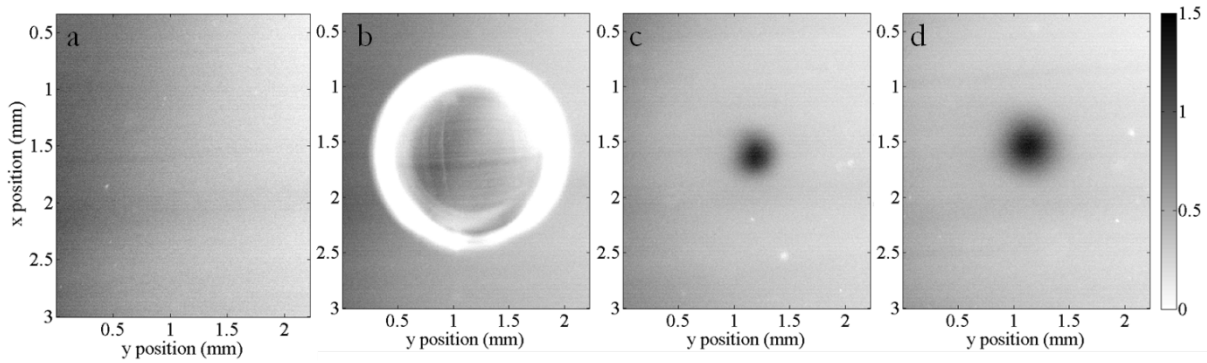

Figure 3- Example of raw recorded sequence by the CCD camera (d_b=1.45 mm, Re=336, water-ethanol 20%w/w solution). The colorbar represents the oxygen concentration in mg/L. Δt=1s between two neighboring images

Before the bubble passage (**Figure 3**-a), the recorded image presents a uniform oxygen concentration of about 0-0.5 mg/L since the solution has been previously deoxygenated by nitrogen. Note that the uniform concentration profile is corrupted, as visible in **Figure 3**-a, by the Beer Lambert absorption of the laser light (laser flashing from the right to the left side in **Figure 3**). There is thus an attenuation of the laser light along its trajectory in the liquid phase that degrades the oxygen concentration measurement. This point will be discussed in Part 5-Image processing. The rise and passage of the bubble through the recording plane are depicted in **Figure 3**-b. The bubble passage can easily be determined due to the high reflection occurring at the gas/liquid interface. Finally, the mass transfer in the wake of the bubble is visualized and recorded at successive instants (at 10 Hz) and is characterized by the dark spot on the two last images (**Figure 3** c-d). Since oxygen is diffusing in the liquid media, the spot tends to widen with time. Based on the recorded images, the evolution of the mass transfer in the wake of the bubble can thus be easily derived. As a first difference with François *et al.* (2011), it can be noted that the oxygen concentration values obtained in the wake of air bubbles are quite weak (1.5 mg/L maximum) when compared to pure oxygen bubbles (9 mg/L maximum) studied in their work. This imposes to generate only one bubble for each experiment and to deoxygenate the solution after each test to avoid "pollution" in the solution due to the mass transferred by former bubbles.

3. Visualization of the mass transfer as a function of the bubble diameter

In François *et al.* (2011), it has been observed that for spherical bubbles, the diffusion spot was circular and presented a Gaussian profile. The purpose of this paper is thus to extend this visualization for non spherical configurations. It is indeed well known that in several industrial applications, non-spherical bubbles are encountered. For instance in aeration systems, the typical equivalent bubble diameter is usually around 2-5 mm (Motarjemi and Jameson, 1978) leading to non-spherical systems. To compare results, all the experiments have been conducted within the same liquid phase, *i.e.* a water-ethanol 20%w/w solution with 25 mg/L of Ruthenium complex at 20°C (see characteristics in **Table 1**). The bubble diameters have been changed using different capillaries. Since bubbles considered in this study present an oblate ellipsoidal shape, they are characterized by the classical equivalent bubble diameter (d_b) defined as $(a^2b)^{1/3}$ with a (resp. b) the major (resp. minor) axis of the ellipse (Stöhr *et al.*, 2009). The aspect ratio noted χ defined as $\chi = a/b$ is also considered to characterize the shape of the bubble. Characteristics of the different considered bubbles for these experiments are presented in **Table 2**.

Case	d_b (mm)	χ	Re
1	0.90	1.13	138 Cap 1
2	1.50	1.50	335 Cap 2
3	2.00	1.75	Haricot
4	2.20	1.80	Haricot +
5	2.22	1.81	Double filament
6	2.24	1.21	382 Méduse

Table 2-Diameter, aspect ratio and Reynolds number characterizing the different studied bubbles

The corresponding three dimensional mass transfers are represented in **Figure 4**.

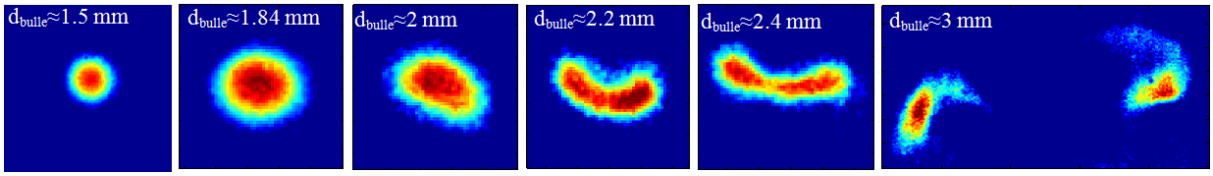

IMAGES 3D DES SEQUENCES POUR DIFFERENTS DIAM DE BULLES

Figure 4- Three dimensional visualization of the mass transfer depending on bubble diameters

Concerning spherical bubbles whose movement is vertical, same conclusions as those obtained by François *et al.* (2011) have been observed. The mass transfer is exclusively contained in the bubble wake with a liquid smoothly flowing around the bubble (Koynov *et al.*, 2005). As a simple extension of the spherical case, when the bubble is slightly ellipsoidal (χ=1.13), the spot presents an ellipsoidal shape too. However this simple behavior of the spot is no longer valid for stronger aspect ratios. The hydrodynamic behavior becoming more complex in the bubble wake implies a distortion of the spot. The spot tends to divide into two parts and the separation of the spot has been observed for d_b≈2 mm. It has to be noted that the deformation of the spot is not due to a change in the bubble path since deformation appears even for a vertical path. As an explanation, it has been numerically observed by Koynov *et al.* (2005) that for some bubbles following a vertical path, depending on the bubble shape, mass transfer can be "trapped in the twin recirculation cells" present in the bubble rear. For zigzagging bubbles, the mass transfer behavior can be clearly more complex. For slightly zigzagging bubbles, two counterrotating spots can be observed as presented in **Figure 4** which is in agreement with the two rotating filaments observed by Yamamoto *et al.* (2008). When the zigzag motion is more pronounced, most of the mass transfer tends to be swept along by the vortex shedding regime as

presented in **Figure 5** (Case 6). Note that in **Figure 5**, the solution was intentionally polluted (initially $[O_2]_{bulk} \neq 0$ mg/L). As a consequence, both mass transfer and hydrodynamic behavior have been observed. After the bubble passage (**Figure 5**-a), the presence of two rotating spots of mass transfer can be slightly distinguished (**Figure 5**-b). The hydrodynamic behavior, characterized by horseshoe type vortices, is clearly visible since it pushes polluting oxygen molecules away and is represented by the brighter area in **Figure 5**-c-d.

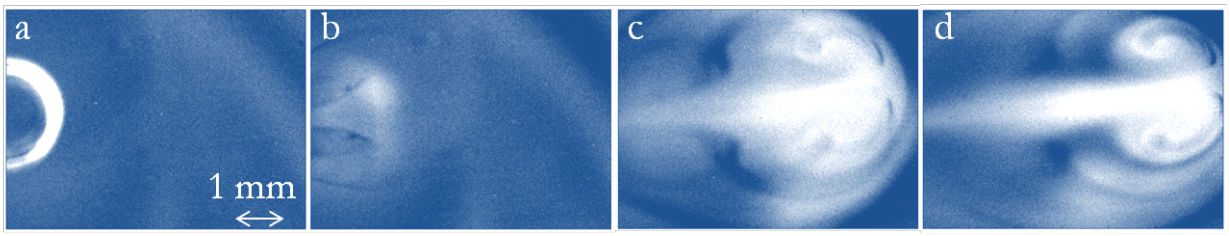

Figure 5- Visualization of the hydrodynamic behavior on the wake of a zigzagging bubble (Case 6)

For larger bubble diameters, the mass transfer dissipation is becoming too fast to allow an accurate visualization of the phenomenon, mainly due to the limitation of the sampling frequency of the optical system. However, it has been observed by Stöhr *et al.* (2009) that the larger the bubble ($d_b \approx 4$mm), the more tortuous becomes the mass transfer structure.

For this kind of bubbles (bubbles with a non vertical path), the quantification of the mass transfer is delicate first due to the complexity of the hydrodynamic and mass transfer structures in the wake but also to the small amount of images that can be recorded in such cases. Fortunately, such limitations do not occur for smaller bubble diameters (Cases 1 to 5, db ≤ 2 mm).

4. Quantification of mass transfer for non-spherical configurations

According to François *et al.* (2011) and based on a mass balance decomposed along specific domains (∂D, see **Figure 6**), the flow rate of mass transferred by the bubble, F_{O_2}, can be simplified as [2].

$$F_{O_2} = \frac{dm_{O_2}}{dt} \quad [2]$$

With m_{O_2} the mass of oxygen transferred by the bubble.

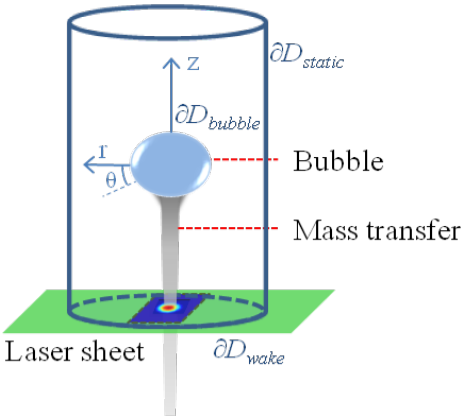

Figure 6- Notations for the mathematical analysis

This simplification can be assumed when considering that, in the domain ∂D_{wake}, at a given distance z sufficiently far away from the bubble, the perturbation induced by the bubble passage has disappeared, leading to the absence of liquid velocity in this domain and that the diffusive flux of oxygen in the bubble wake (∂D_{wake}) is relatively low compared to the interfacial mass transfer $F_{O_2}(\partial D_{bubble})$. From equation [2] and by considering a passage to the limit, [3] can be deduced.

$$F_{O_2} = \frac{dm_{O_2}}{dt} = \lim_{\Delta t \to 0} \frac{\Delta m_{O_2}}{\Delta t} = \lim_{\Delta z \to 0} \frac{\iiint_{V(z)}^{V(z+\Delta z)} [O_2] r dr d\theta dz}{\int_z^{z+\Delta z} dz / U_B} \quad [3]$$

Where U_B is the velocity of the bubble (m/s).

Away from the bubble, it makes also sense to assume that the variation of $[O_2]$ along z can be neglected compared to the variation along r, leading to $[O_2](r,\theta)$.

In the spherical case, the spherical shape of the spot of mass transfer visualized leads to the consideration of a symmetry along the z axis, leading to $[O_2](r)$. Since this symmetry does not hold for non spherical bubbles, a more general formulation is proposed in [4].

$$F_{O_2} = \frac{dm_{O_2}}{dt} = \lim_{\Delta z \to 0} \frac{\int_z^{z+\Delta z} dz \iint [O_2] r dr d\theta}{\int_z^{z+\Delta z} dz / U_B} = U_B \iint [O_2] r dr d\theta \quad [4]$$

Based on [4], the quantification of the mass flowrate is derived from the bubble velocity than can be easily determined using the high speed camera images and from the value of the integral $\iint [O_2] r dr d\theta$. To estimate this integral in a simpler manner, a discrete sum of the concentration values of interest weighted by the pixel surface has been considered [5].

$$\iint [O_2] r dr d\theta \approx \sum_i [O_2]_i \delta^2 \quad [5]$$

Where $[O_2]_i$ is the oxygen concentration of the ith pixel on the recorded image (see **Figure 3**-c-d) and δ is the length of any square pixel (of surface δ^2). When considering this expression for the mass transfer quantification, no assumption on the shape of the spot has been considered and is thus applicable for all the cases presented in **Figure 4**. Based on the knowledge of F_{O_2}, other parameters characterizing the gas/liquid mass

transfer can be deduced such as the flux density j_{O_2} [6] or the liquid side mass transfer coefficient [7].

$$j_{O_2} = \frac{F_{O_2}}{\Pi d_B{}^2} \quad [6]$$

$$k_L = \frac{j_{O_2}}{[O_2]_{saturation} - [O_2]_{bulk}} \quad [7]$$

With $[O_2]_{saturation}$ and $[O_2]_{bulk}$ oxygen concentrations at saturation and far away from the mass transferred by the bubble, respectively.

The main challenge consists thus in the determination of the integral $\iint [O_2] r dr d\theta$ which requires some preliminary image processing before achieving an accurate quantification of the mass transfer in the wake of the rising bubble.

5. Image processing

Since oxygen concentration fields recorded for these measurements are weaker than the one presented by François *et al.* (2011), further investigations on image processing has been required. As mentioned in Part 2.2, even if the solution presents a uniform oxygen concentration, the concentration field on the recorded images is not homogeneous due to the Beer Lambert absorption. This phenomenon is illustrated in **Figure 7**. This figure depicts a three dimensional representation of the hole image studied in **Figure 3**-d. The laser source is flashing from the right side (y=5mm) toward the left side (y=1mm). The Beer Lambert absorption is clearly visible since a difference of about 1 mg/L has been observed between the two opposite sides of this

image. Such a phenomenon could dramatically distort the results since the range of Beer Lambert absorption is in the same order of magnitude than that of the mass transfer and must be corrected.

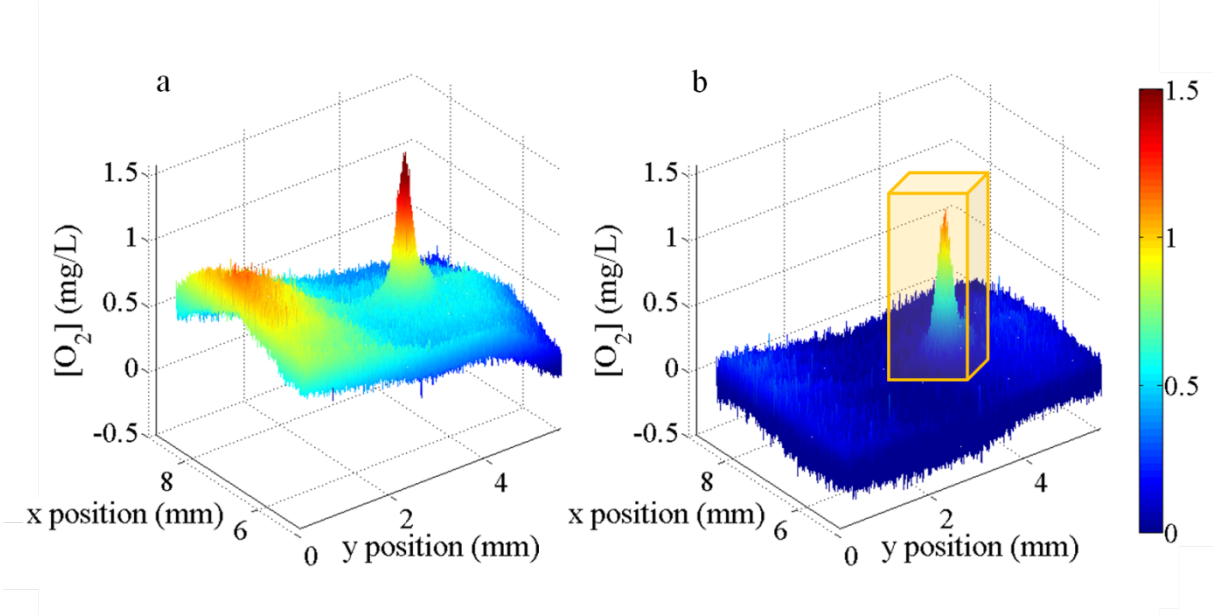

Figure 7- Beer Lambert absorption before (a) and after (b) image processing- Colorbar in mg/L

Based on **Figure 7**-a, it can be also noted that the recorded concentrations present also a non-homogeneity along the y-axis (see especially the curvature on the left side, y=1mm, in **Figure 7**-a). A possible explanation is a widening of the laser sheet. It has been already observed that this dispersion presented a lower impact than the Beer Lambert absorption (difference of about 0.2 mg/L between the top, x=9mm, and the bottom, x=6mm, of the picture).

To correct both phenomena of dispersion, the image processing consisted first of subtracting to the raw image (such as **Figure 7**-a) a reference image corresponding to an image before the bubble passage, with thus a uniform oxygen concentration close

to 0 mg/L (such as **Figure 3**-a). An example of corrected image is depicted in **Figure 7**-b. Since the dye is supposed to be homogeneously dissolved in the liquid phase, the bulk of the corrected image presents an almost uniform concentration at about 0 mg/L. However, it can be noted that the presence of additional noise on the recorded image makes the boundary between the mass transferred by the bubble and this noise not easy to define.

To determine this boundary, the noise level has been estimated using a part of the image free from transfer spot (whole image without the zone included in the parallelepiped with mass transfer in **Figure 7**-b). It can be seen (*cf.* **Figure 8**) from the noise histogram (black dashed line) that the noise can be reasonably assumed to be Gaussian (solid line) whose mean and variance σ^2 can be easily determined.

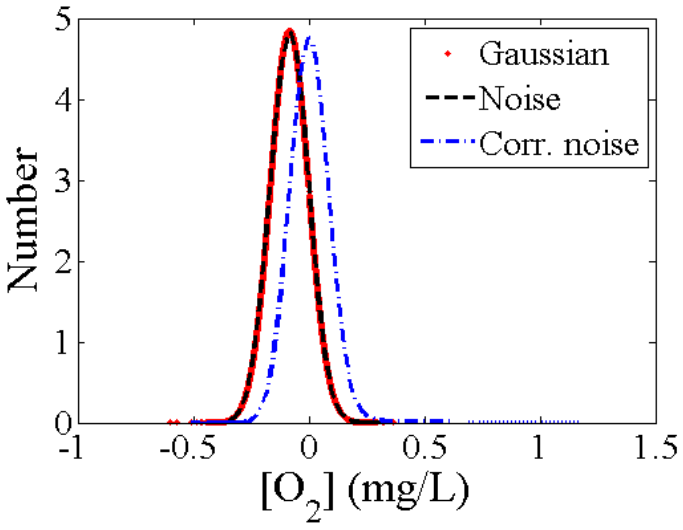

Figure 8- Noise profiles before (dashed line) and after (dash-dot line) correction

As illustrated in **Figure 8**, the mean value of the noise could differ from the expected 0 value. Different explanations can be proposed to reach this conclusion: presence of

additional noise such as the presence of some particles for instance, choice of the reference image, varying laser source intensity, calibration curve *etc.*. An offset is thus considered to shift all the values of the image (including the zone with mass transfer) to obtain the mean 0 (see dash-dot line in **Figure 8**). Note that this step allows also correcting the non-homogeneity of the laser intensity.

However, a precision is needed concerning the noise Gaussian profile. This profile has been only obtained for fully deoxygenated solutions when only a single bubble has been generated. In the case of previous bubbles passage, residual mass transfer from these bubbles can appear on the recorded image (see **Figure 9**-a). When considering this residual transfer, the noise profile is obviously no longer Gaussian (see **Figure 9**-b). Specific cares must thus be taken into account while achieving the experiments to avoid such configurations.

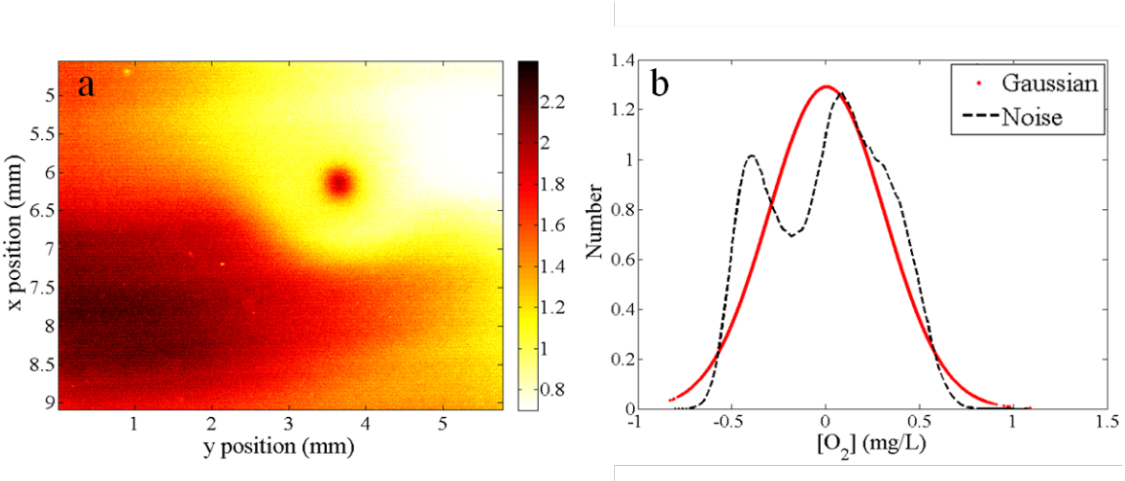

Figure 9- Noise level compared with a Gaussian profile for a polluted solution in oxygen. Colorbar in mg/L

Assuming the Gaussian profile of the noise, a threshold is fixed as defined in [8] to determine the boundary between the noise of the image and the mass transferred by the bubble.

$$\begin{aligned} &For\ [O_2] \geq \lambda \times \sigma, \quad [O_2] \\ &For\ [O_2] \leq \lambda \times \sigma, \quad [O_2] = 0 \\ &\lambda \in \{0, 1, 2, 3, 4, 5\} \end{aligned} \qquad [8]$$

Where σ is the standard deviation of the Gaussian profile of the noise and λ is the threshold factor. All oxygen concentrations superior to $\lambda \times \sigma$ are thus considered as mass transfer, the other values being fixed to 0 mg/L. The choice of the threshold factor is crucial since it will directly impact the quantification of the mass and depends on the image quality. An example of visualization of the final corrected image for two different threshold factors is proposed in **Figure 10**. **Figure 10**-a represents the raw image (λ=0). It can be noted that the background of the image is at about 0.2 mg/L due to the residual noise and not to the mass transferred by the bubble. After correction (**Figure 10**-b), the impact of the noise has been limited, pixels with a non null oxygen concentration being now considered as mass transfer. The threshold factor has been chosen for each recorded image to minimize the residual noise.

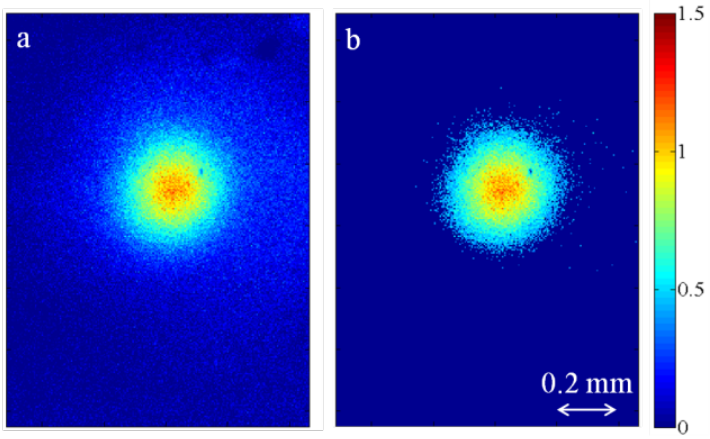

Figure 10- Visualization of corrected images for λ=0 (a) and λ=4 (b). Colorbar in mg/L

Based on equation [5] and the final corrected image (such as **Figure 10**-b), the accurate characterization of the mass transfer is thus feasible.

6. Results and discussion

6.1. Application to an ellipsoidal configuration

The new approach proposed in this paper has been first tested in the closest case to the spherical configuration by considering an ellipsoidal case. Image processing and mass transfer quantification have been performed for each spot recorded by the CCD Camera after the bubble passage (a recording every 1/10s). An example of corrected images is represented in **Figure 11**. **Figure 11**-a and **Figure 11**-b correspond to Cases 2 and 3 in **Table 2** respectively. **Figure 11**-c represents another liquid composition to will be detailed in the following section.

As mentioned above, for the Case 1 (d_b=0.9mm, χ=1.13), the spot shape is slightly ellipsoidal and starts to be deformed for Case 2 (d_b=1.5mm, χ=1.50) and it tends to widen with time due to the diffusive process

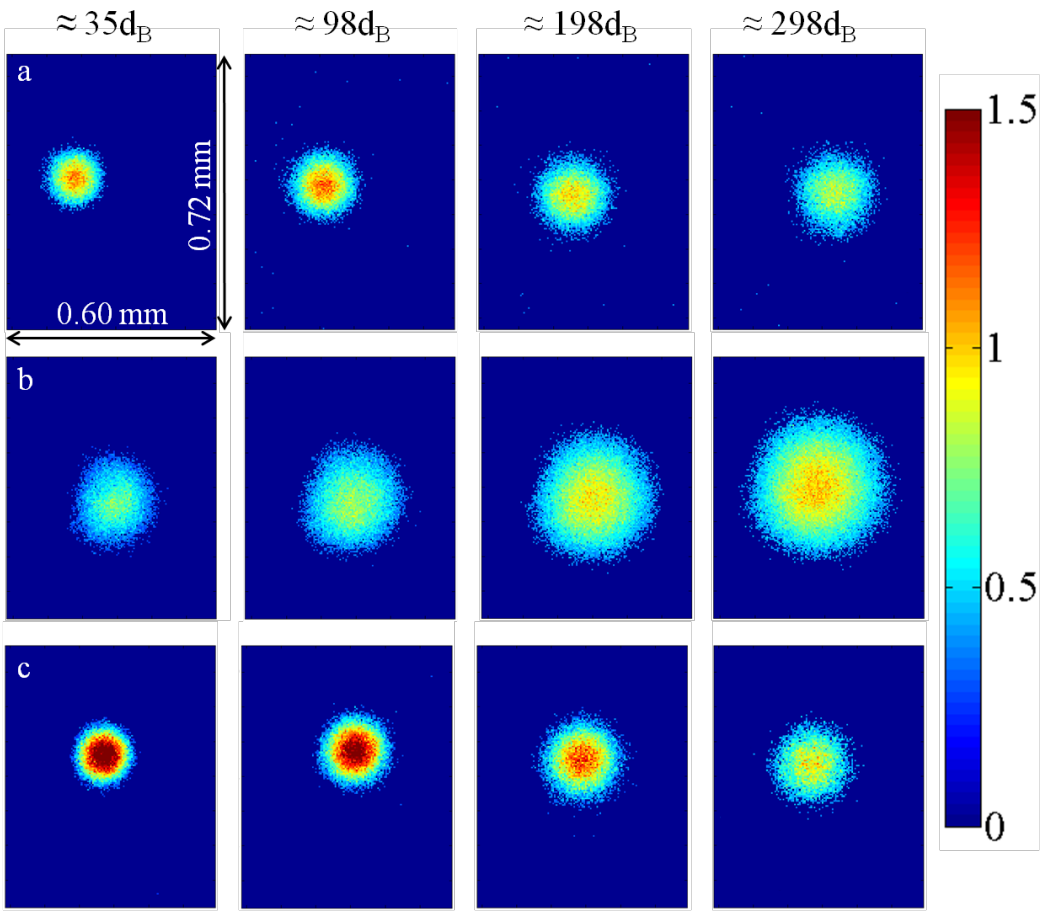

Figure 11- Example of corrected images for Case 1 (a), Case 2 (b) and a water-20%ethanol-10%glycerol solution at different distances from the bubble. Colorbar in mg/L.

410

A typical example of flux density, determined using equations [4], [5] and [6], is represented in **Figure 12**. It has been observed for all experiments that the flux density behavior could be decomposed in three main parts.

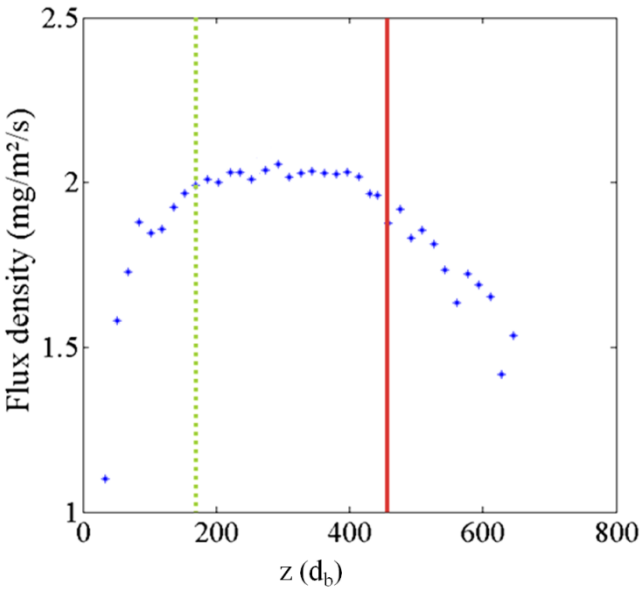

Figure 12- Example of flux densities of mass transfer evolution as a function of the number of bubble diameters

On the presented example, the first one ($z<180\ d_b$ in **Figure 12**) is characterized by an increase of the estimated mass transfer. This augmentation can be explained by the fact that the bubble is not far enough to satisfy the hypothesis of absence of liquid motion. The mathematical approach for determining this flux density is thus not available in this region. Moreover, it has been observed that the bubble shadow could distort measurements on the first few images after the bubble passage in the focal plane.

Then at a sufficiently large distance to the bubble ($z>180\ d_b$ in **Figure 12**), perturbations due to the bubble passage weakened, and thus the expected zone of constant flux density is observed.

After hundreds of bubble diameters, the flux density decreases ($z>450d_b$ in **Figure 12**). This diminution is due to the fixed threshold ($\lambda\times\sigma$) setting the limit between mass transfer and the noise. At these distances, the mass transfer spot becomes spread and of low amplitude, which makes it difficult to identify. Calculations must obviously be considered in the zone of constant flux. The flux density profile in the wake of the bubble seems to confirm the reliability of the proposed approach. However, to insure it and since there is no possible direct comparison, the liquid side mass transfer coefficient k_L has been determined (using equation [7]) and compared to the theoretical values of the Frössling (fully contaminated bubbles) [9] and the Higbie (clean bubbles) [10] models (Higbie, 1935; Frössling, 1938).

$$k_{L_F} = \frac{D_{O_2}}{d_b}(2 + 0.6\,\mathrm{Re}^{0.5}\,Sc^{0.33}) \quad [8]$$

$$k_{L_H} = \frac{D_{O_2}}{d_b}(1.13\,\mathrm{Re}^{0.5}\,Sc^{0.5}) \quad [8]$$

With D_{O_2} the diffusion coefficient of oxygen in the liquid phase and Sc the Schimdt number.

The values of D_{O_2} are those reported by Jimenez *et al.* (2012) where the same optical system and solutions have been considered. The experimental values of k_L compared to the literature are presented in **Table 3**.

Case	k_L exp (m/s)	k_L Higbie (m/s)	k_L Frössling (m/s)	$k_L{}^a$ (m/s)	$k_L{}^b$ (m/s)
2	2.49×10^{-4}	7.09×10^{-4}	1.35×10^{-4}	$\approx2.00\times10^{-4}$	-
3	4.31×10^{-4}	6.48×10^{-4}	1.22×10^{-4}	$\approx2.82\times10^{-4}$	$\approx4.64\times10^{-4}$

Table 3-Comparison of the liquid side mass transfer coefficients with literature
[a] Kück et al. (2010) for water-oxygen results
[b] Kück et al. (2010) for water-oxygen-1% ethanol results

As expected, the experimental values of liquid side mass transfer coefficients are comprised between the two theoretical extremes cases. This supposes that the bubble is partially contaminated which makes sense since water is scarcely considered as extra pure (Alves *et al.*, 2005) and since the presence of the ethanol and the dye alters also the bubble contamination. Moreover, experimental results have been compared to those reported by Kück *et al.* (2010) who managed k_L measurements using the PLIF technique in the axisymmetric wake of rising bubble in water and water+ethanol solutions. As a first comment, it can be noted that as expected the presence in ethanol indubitably lowers the surface tension of the liquid phase in comparison with a pure water solution (see **Table 1**) and other measurements have concluded that the addition of the fluorescent dye does not modify the liquid properties. The mass transfer is thus supposed to be lowered too as it has been reported by some experiments (Maceiras *et al.*, 2007). However this trend has not been observed by Kück *et al.* (2010) whose experiments are the closest to those presented in this paper. As shown in **Table 3**, they obtained an improved local mass transfer by adding a small amount of ethanol in the solution. A possible explanation to such conclusions is the presence at the bubble interface of surface tension gradients and thus of a Maragoni effect (Alves *et al.*, 2005; Jamnongwong *et al.*, 2010). Further efforts to locally identify the impact of ethanol on the mass transferred by a single bubble have thus to be investigated. Anyway, the presence in ethanol does not distort neither the possibility to analyze the impacts of bubble diameters/liquid composition on the mass transfer nor the reliability of the

proposed technique. It can also be noted that surface tension ranges similar to those presented in this paper can be encountered in some industrial purposes (see Pothof *et al.*, 2012).

6.2. Impact of the bubble diameters on the flux density

Based on the results presented in Part 6.1, the same calculation has been performed for other configurations than the ellipsoidal one (see the different configurations in **Figure 4**). The main purpose is thus to quantify the impact of the bubble diameter on the flux density behavior in its wake. An example of this impact is proposed in **Figure 13**. The global behavior of the flux density is similar for the two considered cases (Case 1, d_b=0.9 mm, χ=1.13 and Case 2, d_b=1.5 mm, χ=1.5 **Figure 11** a and b) which includes a first part of increase of flux density, then a constant flux density zone and finally a progressive decrease. However, the larger the bubble, the farer the distance to satisfy the absence of liquid motion hypothesis and the higher the transfer. Francois *et al.* (2011) proposed the formula $z_C=20\sqrt{Re}$ as a indicator of the distance (expressed in bubble diameter) to reach the constant flux zone. When applying this formula for the two considered cases presented in **Figure 13**, distances of about 235 and 367 d_b have been predicted for d_b=0.9 mm and 1.5 mm respectively. These predictions are in very good agreement with experiments which tends to confirm that this formula could be a pertinent indicator for non spherical configurations too.

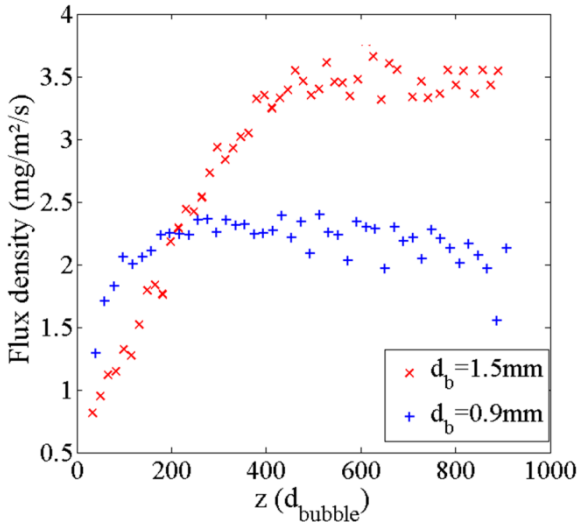

Figure 13- Impact of the bubble diameter on the flux density (Cases 2 and 3)

As mentioned above, for bubble diameters up to 2 mm, the mass transfer dissipation in the bubble wake is too strong and the zone of constant flux is not reached.

6.3. Impact of the liquid composition on the flux density

Since the same behavior on the flux density has been observed for different bubble diameters, experiments have been focused on the impact of the liquid composition on the bubble hydrodynamic and mass transfer. To determine thus the impact of the liquid composition, the same gas injection system as that used for Case 1 (d_b=0.9 mm, χ=1.13) has been considered. The different tested liquid media are briefly summarized in **Table 1**. Same tendencies as those reported by Jamnongwong *et al.* (2010) have been observed concerning the change in surface tension (except for the solution with 1 g/L of Glucose whose surface tension is supposed to be lower). The impact of viscosity is considered by addition of glycerol.

Some results concerning the hydrodynamic behavior for these different configurations are presented in **Table 4**.

Composition		d_b (mm)	χ	U_b (cm.s^{-1})	j_{O_2} (mg.s^{-1}.m^{-2})
Water-Ethanol 20%w/w		0.9	1.13	16.8	1.95
+ Salt	1 g/L	0.86	1.09	17.2	0.76
	5 g/L	0.85	1.09	17.1	0.23
+ Glucose	0.5 g/L	0.95	1.11	17.5	0.53
	1 g/L	-	-	-	-
+ Glycerol	10% w/w	0.97	1.07	15.4	1.55
	25% w/w	0.95	1.05	11.2	1.55

Table 4- Results for the different considered liquid media

505

Experiments conducted with 1 g/L of glucose in the solution leaded to an opaque and cloudy solution. Even images recorded by the high speed camera were difficult to analyze and PLIF measurements were impossible to be performed. For the other cases, concerning the bubble diameter and aspect ratio, taking into account the

510 uncertainties for these measurements (about 10%) and the bubble reproducibility, it seems that the liquid composition does not alter dramatically these parameters. This conclusion is in agreement with those reported by Jamnongwong *et al.* (2011). Changes in viscosity are obviously the main parameter influencing the bubble velocity. By overlooking the glycerol case, all the other tested solutions seem to present similar

515 hydrodynamic characteristics similar to those of the Case 1 (Water-Ethanol 20%w/w). However, the flux density behavior highly differs from a liquid solution to another. Such a phenomenon is illustrated in **Figure 14**.

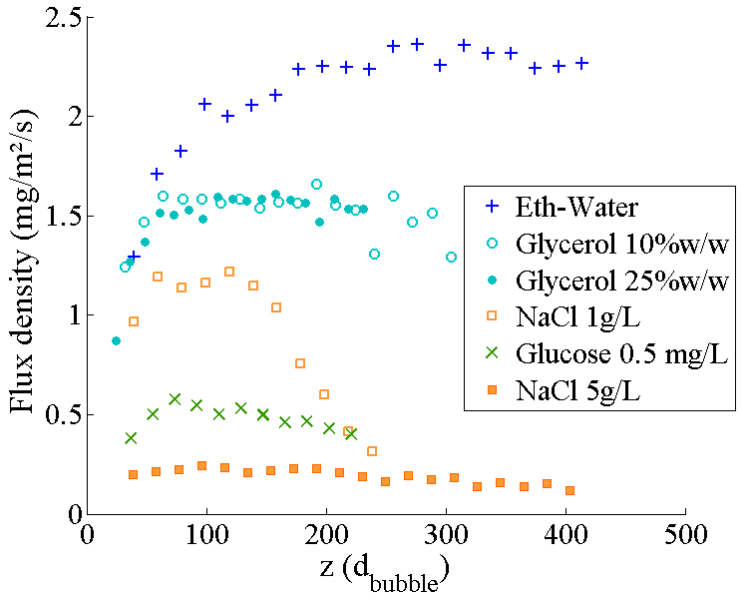

Figure 14- Impact of the liquid composition of the flux density transferred by the bubble

Concerning the glycerol, as mentioned above, the bubble being slowed down by the viscosity, the residence time between the bubble and the liquid is longer. On the recorded images, as visible in **Figure 11**-c, the maximum oxygen concentration observed is thus higher (about 2 mg/L) than in the other compositions. This conclusion is strengthened by the comparison of the values of the integral $\iint [O_2] r dr d\theta$. This term represents thus the diffusive process of the bubble without any consideration of d_b or U_b. It has been observed that this term was effectively higher when glycerol was introduced in the solution compared with the water-ethanol solution (20% and 46% higher for 10%w/w and 25%w/w glycerol respectively). As observed by Bothe *et al.* (2005), the higher the Schmidt number, the thinner the liquid boundary layer around the bubble. Concentration gradients at the bubble surface could thus be more important in the viscous solution. However, due to the diminution of the bubble rise, the final flux density is lower (≈21%) than in the water-ethanol

solution. When considering the addition of salt in the solution, the first observed phenomenon is a decrease of the fluorescence level (40% of decrease for the 5g/L solution compared with the water-ethanol solution). Due to the dye composition, it tends to be less soluble in ionic solutions meaning that the contamination of the bubble could be higher too. The second observation is that the oxygen concentration field on the recorded images is so weak (always < 0.8 mg/L) that there are just few images where the region of constant flux can be observed before the estimated flux decreases due to the threshold. As a consequence, the flux density is dramatically lower than in the initial solution (61% and 88% lower with 1 and 5 g/L respectively).

Concerning the impact of the glucose, contrary to the 1 g/L solution, with only 0.5 g/L the cloudy aspect has disappeared. However, similar conclusions as those formulated for the salt can be conducted. A decrease of about 73% of the flux density has been observed.

It can thus be observed that small changes in the liquid composition could dramatically alter the behavior of the mass transferred in the bubble wake. Except for the glycerol case, a net diminution of the oxygen concentration fields recorded has been observed for all the other tested cases. Such phenomena could be attributed to a decrease of diffusion coefficients due to the surfactants accumulation at the bubble surface (Jamnongwong *et al.*, 2010; Sardeing *et al.*, 2006; Painmanakul *et al.*, 2005). For viscous media, in the tested cases, the bubble velocity diminution seems to be the main parameter inducing a decrease of the k_L.

7. Conclusion

An extension of the work presented by François *et al.* (2011) has been proposed to obtain a better comprehension of the mechanisms occurring during the mass transfer process of a rising bubble. As a first step, the technique has been extended to non-spherical bubbles. It has been observed that the bubble shape is a crucial parameter. Depending on it, the mass transfer can be either characterized by a single or two counterrotating filaments. Based on the proposed technique, the three dimensional representation of the mass transfer has been achieved for equivalent bubble diameters up to 2mm. A specific experiment allowed the relevant visualization of the vortex shedding regime occurring in the wake of zigzagging bubbles. For larger bubble diameters, the dissipation due to the complex hydrodynamic behavior in the wake is too strong to be visualized. Based on the three-dimensional representation of the oxygen concentration field in the bubble wake, a mathematical approach has been proposed to accurately determine the main parameters characterizing mass transfer (flux density, liquid side mass transfer coefficient). The main advantage of this approach is that it does not account the shape of the mass transfer. Asymmetric configurations can thus be analyzed. The hypothesis of no liquid velocity in the bubble wake is satisfied for the studied cases but further efforts have to be done to consider slightly zigzagging bubbles. Based on this approach, the impact of the liquid composition has been studied by adding salt, glucose or glycerol to the liquid phase. One of the main advantages of the method presented in this paper consists of a local analysis of the liquid composition, at the bubble scale. Very few changes in the liquid composition could drastically alter the behavior of the transferring bubble. A

significant diminution of the visualized oxygen concentration fields in the bubble wake has been observed in most cases. This diminution is assumed to be due to additional resistance at the bubble interface that hinder the mass transfer. The change in viscosity conducts to other conclusions: the mass transferred in the bubble wake is enhanced in viscous media but limited by the rise velocity. Further efforts will be investigated to widen the liquid composition range (especially by considering a mixture of the different added components) and to be closer to most industrial purposes. Quantitative measurements also have to be performed in more complex configurations such as bubble trains. Tests with fluorescent dyes directly soluble in water are also to be scheduled to allow an accurate quantification of the local impact of ethanol on the mass transfer.

Nomenclature

	a	Major axis of oblate ellipsoidal bubble, mm
595	b	Minor axis of oblate ellipsoidal bubble, mm
	d_B	Equivalent bubble diameter, mm
	F_{O_2}	Oxyegn mass flowrate, g/s
	I_Q	Fluorescence level in presence of quencher, grey level
	I_0	Fluorescence level in absence of quencher, grey level
600	j_{O_2}	Flux density, $mg.m^{-2}.s^{-1}$
	k_L	Liquid side mass transfer coefficient, m.s-1
	K_{SV}	Stern Volmer constant, L/mg
	m_{O_2}	Mass of transferred oxygen, g
	$[Q]$	Quencher (oxygen) concentration, mg/L
605	r	radius, m
	Re	Reynolds number
	t	Time, s
	U_B	Bubble velocity, m/s
	z	Distance to the bubble, bubble diameter
610	χ	Aspect ratio of the bubble, a/b
	μ	Viscosity, Pa.s
	ρ	Density, $kg.m^{-3}$
	θ	grade
	δ	length of a pixel on the recorded image, m

615	σ^2	Variance
	λ	Threshold factor
	σ	Surface tension, $mN.m^{-1}$

Figure Caption

Table Caption

Table 4 Results for the different considered liquid medi

References

Alves, S.S., Orvalho, S.P., Vasconcelos, J.M.T., 2005. Effect of bubble contamination on rise velocity and mass transfer. Chemical Engineering Science 60, 1-9.

Bel Fdhila, R., Duineveld, P.C., 1996. The effect of surfactant on the rise of a spherical bubble at high Reynolds and Peclet numbers. Physics of Fluids 8, 310-321.

Bork, O., Schlueter, M. and Raebiger, N., 2005. The Impact of Local Phenomena on Mass Transfer in Gas-Liquid Systems. Canadian Journal of Chemical Engineering 83, 658–666.

Bothe, D., Warnecke, H.J., 2005. VOF-simulations of rising air bubbles with mass transfer to the ambient liquid. 10th Workshop on Transport Phenomena in Two-phase Flow.

Brücker, C., 1999. Structure and dynamics of the wake of bubbles and its relevance for bubble interaction. Physics of Fluids 11, 1781-1796.

Calderbank, P.H., Lochiel, A.C., 1964. Mass transfer coefficients, velocities and shapes of carbon dioxide bubbles in free rise through distilled water. Chemical Engineering Science 19, 485-503.

Colombet, D., Legendre, D., Cockx, A., Guiraud, P., Risso, F., Daniel, C., Galinat, S., 2011. Experimental study of mass transfer in a dense bubble swarm. Chemical Engineering Science 66, 3432-3440.

Crimaldi, J., 2008. Planar laser induced fluorescence in aqueous flows. Experiments in Fluids 44, 851-863.

Dani, A., Guiraud, P., Cockx, A.,2007. Local measurement of oxygen transfer around a single bubble by planar laser-induced fluorescence. Chemical Engineering Science 62, 7245-7252.

de Vries, A.W.G., Biesheuvel, A., van Wijngaarden, L., 2002. Notes on the Path and Wake of a Gas Bubble Rising in Pure Water. International Journal of on MultiPhase Flow, 28, 1823-1835.

François, J., Dietrich, N., Guiraud, P., Cockx, A., 2011. Direct measurement of mass transfer around a single bubble by micro-PLIFI. Chemical Engineering Science 66, 3328-3338.

Frössling, N., 1938. Über die Verdünstung fallenden Tropfen. Gerlans Beitage Geophysik 52, 170-216.

Geddes, C.D., 2001. Optical halide sensing using fluorescence quenching: theory, simulations and applications-a review. Meas Sci Technol 12, R53-R88.

Hanyu, K., Saito, T., 2010. Dynamical mass-transfer process of a CO2 bubble measured by LIF/HPTS visualisation and photoelectric probing. Canadian journal of chemical engineering 88, 551-560.

Herlina, Jirka, G.H., 2004. Application of LIF to investigate gas transfer near the air-water interface in a grid-stirred tank. Experiments in Fluids 2004, 341-349.

Higbie, R., 1935.The rate of absorption of a pure gas into a still liquid during short periods of exposure, Transactions of The American Institution Chemical Engineers 35, 36-60.

Jamnongwong, M., Loubiere, K., Dietrich, N, Hébrard, G., 2010. Experimental study of oxygen diffusion coefficients in clean water containing salt, glucose or surfactant: Consequences on the liquid-side mass transfer coefficients. Chemical Engineering Journal 165, 758-768.

Jimenez, M., Dietrich, N., Cockx, A., Hébrard, G., 2012. Experimental study of O_2 diffusion coefficient measurement at a planar gas–liquid interface by planar laser-induced fluorescence with inhibition. AIChE J., doi: 10.1002/aic.13805

Koynov, A., Khinast, J. G., Tryggvason, G., 2005. Mass transfer and chemical reactions in bubble swarms with dynamic interfaces. AIChE J. 51, 2786-2800.

Kück, U.D., Schlüter, M., Räbiger, N., 2010. Investigation on Reactive Mass Transfer at Freely Rising Gas Bubbles Experimental Methods for Multiphase Flows. 7th International Conference on Multiphase Flow - ICMF 2010 Proceedings.

Lakowicz J.R.,1999. Advanced topics in fluorescence quenching. In: Principles of Fluorescence Spectroscopy, 2nd ed. New York, NY: Plenum 267-289.

Lindken, R., Merzkirch, W., 2000. Velocity measurements of liquid and gaseous phase for a system of bubbles rising in water. Experiments in Fluids 29, S194-S201.

Lunde, K., Perkins, R. J., 1997. Observations on wakes behind spheroidal bubbles and particles. FEDSM'97-3530, ASMEFED Summer Meeting.

Ma, Y., Cheng, H., Yu, G., 1999. Measurement of Concentration Fields near the Interface of a Rising Bubble by Holographic Interference Technique. Chinese Journal of Chemical Engineering 7, 363-367.

Maceiras, R., Santana, R., Alves, S., 2007. Rise velocities and gas–liquid mass transfer of bubbles in organic solutions. Chemical Engineering Science 62, 6747-6753.

Madhavi, T., Golder, A.K., Samanta, A.N., Ray, S., 2007. Studies on bubble dynamics with mass transfer, Chemical Engineering Journal 128, 95-107.

Motarjemi M., Jameson, G.J., 1978. Mass transfer from very small bubbles—the optimum bubble size for aeration. Chemical Engineering Science 33,1415-23.

Painmanakul,P., Loubière, K. Hébrard, G., Mietton-Peuchot, M., Roustan, M. 2005. Effect of surfactants on liquid-side mass transfer coefficients. Chemical Engineering Science 60, 6480-6491

Pothof, I., Schuit, A., Clemens, F. 2012. The Influence of Surface Tension on Air-Water Flows. Journal of Hydraulic Engineering..doi: 10.1061/(ASCE)HY.1943-7900.0000637

Riethues, M., Buchholz, R., Onken, U., Baumgärtl, H., Lübbers, D.W., 1986. Determination of oxygen transfer from single air bubbles to liquids by oxygen microelectrodes. Chemical Engineering and Processing: Process Intensification 20, 331-337.

Sanada, T., Shirota, M., Watanabe, M., 2007. Bubble wake visualization by using photochromic dye. Chemical Engineering Science 62, 7264–7273.

Sardeing, R., Painmanakul, P., Hébrard, G., 2006. Effect of surfactants on liquid-side mass transfer coefficients in gas–liquid systems: A first step to modeling, Chemical Engineering Science 61, 6249-6260.

Stern, O., Volmer, M., 1919. On the quenching time of fluorescence. Physik Z 20, 183-188.

Stöhr, M., Schanze, J., Khalili, A., 2009. Visualization of gas–liquid mass transfer and wake structure of rising bubbles using pH-sensitive PLIF. Experiments in Fluids 47, 135-143.

Tachibana, R., Saito, T., 2010. Dynamical Vortex-shedding from a Zigzagging Rising Bubble Fluid Structure Interactions. 7th International Conference on Multiphase Flow-ICMF 2010 Proceedings.

Wolff, L.M, Liu, Z.C, Hanratty, T.J, 1991. A fluorescence technique to measure concentration gradients near an interface. In Gas Transfer at Water Surfaces. Wilhelms SC, Gulliver JS. ASCE Press: New York, 210-218.

Yamamoto, M., Yamada, M., Morikawa, K., Sanada, T., Saito, T. 2008. Coupling mechanism between liquid phase motion and mass transfer around single rising bubbles by using PIV/LIF. 14th Int Symp on Applications of Laser Techniques to Fluid Mechanics, Lisbon,Portugal.

Zhang, Y., Sam, A., Finch, J.A., 2003. Temperature effect on single bubble velocity profile in water and surfactant solution. Colloids and Surfaces A: Physicochemical and Engineering Aspects 223, 45-54.